

Development of the Glenn-Heat-Transfer (Glenn-HT) Computer Code to Enable Time-Filtered Navier Stokes (TFNS) Simulations and Application to Film Cooling on a Flat Plate Through Long Cooling Tubes

Ali Ameri

The Ohio State University, Columbus, Ohio 43210

Vikram Shyam

National Aeronautics and Space Administration Glenn Research Center, Cleveland, Ohio 44135

David Rigby

Vantage Partners, LLC, Brook Park, Ohio 44142

Phillip Poinsette

National Aeronautics and Space Administration, Glenn Research Center, Cleveland, Ohio 44135

Douglas Thurman

U.S. Army Research Laboratory, Glenn Research Center, Cleveland, Ohio 44135

Erlendur Steinthorsson, A & E Consulting, Inc., Pepper Pike, Ohio 44124

Abstract

Computational fluid dynamics (CFD) analysis using Reynolds-averaged Navier-Stokes (RANS) formulation for turbomachinery-related flows has enabled improved engine component designs. RANS methodology has limitations that are related to its inability to accurately describe the spectrum of flow phenomena encountered in engines. Examples of flows that are difficult to compute accurately with RANS include phenomena such as laminar/turbulent transition, turbulent mixing due to mixing of streams, and separated flows. Large eddy simulation (LES) can improve accuracy but at a considerably higher cost. In recent years, hybrid schemes that take advantage of both unsteady RANS and LES have been proposed. This study investigated an alternative scheme, the time-filtered Navier-Stokes (TFNS) method applied to compressible flows. The method developed by Shih and Liu was implemented in the Glenn-Heat-Transfer (Glenn-HT) code and applied to film-cooling flows. In this report the method and its implementation is briefly described. The film effectiveness results obtained for film cooling from a row of 30° holes with a pitch of 3.0 diameters emitting air at a nominal density ratio of unity and two blowing ratios of 0.5 and 1.0 are shown. Flow features under those conditions are also described.

Nomenclature

d	diameter
DR	density ratio
e	internal energy per unit mass
G	time filter defined in Equation (2)
k	turbulence kinetic energy
L	length
M	blowing ratio
p	pressure
Q	heating rate

q_i	heat fluxes
R	universal gas constant
T	temperature
t	time
Tu	free-stream turbulence intensity
u	velocity
x	streamwise coordinate measured from hole trailing edge
y	spanwise coordinate
z	normal to the plate coordinate
Δ_T	temporal filter width
ε	turbulence dissipation rate
η	effectiveness defined in Equation (24)
η_1	effectiveness defined in Equation (25)
κ	thermal conductivity
μ	viscosity
ν	kinematic viscosity
ρ	density
τ_{ij}	unresolved turbulent stresses
ϕ	turbulence variable
ω	specific dissipation rate
$(\dots)_t$	temporal derivative
$(\dots)_i$	spatial derivative

Subscripts

T	turbulent value
aw	adiabatic wall
c	coolant
r	recovery
∞	inlet total

Superscripts

$-$	time filtered value
\sim	density weighted value

1-Introduction

High operating pressure ratios as well as increased turbine inlet total temperatures are expected to be the hallmarks of NASA's N+3 engines. Cooling of blades with film cooling is an effective means of insulating blades from hot combustion gases and is thus expected to continue to be an important method for cooling unless materials are developed that can tolerate much higher temperatures. Currently, the cooling air used for high-pressure turbine cooling comprises approximately 15 percent of the mass flow through the core. This use of cooling air is a loss to the efficiency of the engine and needs to be minimized.

For film-cooling flows in the higher blowing ratio M range ($M > 1.0$) Reynolds-averaged Navier-Stokes (RANS) analysis does not produce accurate solutions (Ref. 1). Argument is made that RANS models are not adequate for film-cooling flows as the unsteady interactions and mixing of the main stream and cooling stream play an important role that are not accounted for by such models. In recent years attempts have been made to model film-cooling flows using large eddy simulation (LES) and detached eddy simulation (DES). Some of these attempts have resulted in computations of cooling

effectiveness but others have used LES to shed light on the physics of film cooling. Guo et al. (Ref. 2) used LES to study the effect of low blowing ratios (0.1 and 0.48) for respective 90° and 30° inclined angles. Their purpose was to investigate the turbulent flow structure and the vortex dynamics for gas turbine blade film cooling. Their work concluded that turbulent flow downstream of the cooling holes is highly anisotropic and also that LES is well suited for such simulations. Tyagi and Acharya (Ref. 3) studied film-cooling physics for a blowing ratio of 0.5 and a short tube with a 1.75 length-to-diameter ratio. They showed good agreement with experimental measurements for velocity distributions downstream of the hole and described the physical features of the flow resulting from the film-cooling flow. More recently, Fujimoto (Ref. 4) used surface-adjusted octree hexahedral meshes to perform LES computations of film-cooling effectiveness. Fujimoto compared his results and the results of a multiblock LES computation with the experimental data of Sinha et al. (Ref. 5) and reported good agreement with the experimental data for a range of blowing ratios.

Computations have been performed on turbine blades to determine both the heat transfer coefficient and the film effectiveness for film cooling using DES, which uses a combined RANS and LES for the blade surface downstream of an internally ribbed slot. One example is the work of Martini et al. (Ref. 6) which ascribes great advantage to using DES over modeling using RANS methods.

In their earlier LES work for film-cooling flows, Peet and Lele (Ref. 7) used a combination of computational fluid dynamics (CFD) codes—an incompressible method for the plenum and the pipe, and a compressible method for the cross stream and the interaction zone. They computed turbulence statistics and effectiveness of the film cooling for a low-blowing-ratio ($M = 0.5$) case. One of the issues often confronted when computing film-cooling flows concerns the effect of the plenum. Plenum modeling and related assumptions are sources of uncertainty. The plenum is often included in the numerical model but the incompressible flow within the plenum reduces the convergence rate of the numerical schemes. This limitation has little to do with engine conditions and is encountered as experimental setups use plena for film cooling. To model the flow realistically the plena have to be included in the computations.

To eliminate the uncertainty associated with using plena, a new film-cooling experiment has been designed, which uses very long film-cooling pipes with length-to-diameter ratios greater than 20 (Ref. 8). This leads to fully developed flow in the pipe and thus requires no further characterization of the pipe flow. In addition, other confounding conditions such as the effect of the plenum exit and pipe length do not enter the experiment or affect computational results.

The work reported herein utilized the experimental conditions described in (Ref. 8) and conducted a numerical study employing a time-filtered Navier-Stokes (TFNS) method. The resulting film-cooling effectiveness distributions were compared to the data reported in Reference 8. The filtering of equations is performed on timescales rather than length scales of turbulence using an algebraic Reynolds stress model as the subfilter model. The underlying model is described by Liu and Shih (Ref. 9) and is further elucidated in References 10 to 12. The subfilter model in the present work does not use wall functions in contrast to what was done with TFNS (or earlier versions of the model). Instead it uses a model version that is integrated all the way to the wall (Ref. 13). This was necessary since the previous uses of TFNS were for combustion computations, so near-wall flows and heat transfer were not emphasized.

1.1 Description of Work

Flow over a flat plate and temperature distribution downstream of film-cooling holes at a 30° inclination and two blowing ratios of 0.5 and 1.0 for a single nominal density ratio DR of unity were simulated. The range of momentum ratios is thus the same as the blowing ratios. Earlier computations (Ref. 1) performed at a blowing ratio of $M = 2$ showed the inadequacy of the $k-\omega$ turbulence model (Ref. 14) at high blowing ratios. In this study, several turbulence models within the Glenn-Heat-Transfer (Glenn-HT) code (Ref. 15) were used for an intermediate blowing ratio of unity. A commercial code CFX and the models within it (shear stress transport (SST) and $k-\epsilon$) were also applied and verified that results are highly dependent on the choice of turbulence model, which is not acceptable.

Elements of the work performed to enable simulation of film cooling using TFNS are as follows:

- (1) Programming and testing of required routines to simulate unsteady flows, including routines to allow long-term averaging of flow quantities, Reynolds stresses, and relevant unsteady boundary conditions.
- (2) Programming the low Reynolds number $k-\epsilon$ and algebraic Reynolds stress model (ARSM) and verifying that they both worked for turbulent flow heat transfer on a plate.
- (3) Programming and testing of the SST model.
- (4) Programming and testing of individual numerical probes, rakes, or a plane of rakes to allow tracking of the flow variables.
- (5) Implementing the TFNS elements (based on the low-Reynolds-number ARSM into the Glenn-HT code).
- (6) Modeling of the long-piped film-cooling-hole geometry.
- (7) Researching and implementing methods to allow efficient domain dicing and subsequent multiprocess simulations.
- (8) Simulating film-cooling flow using RANS and unsteady Reynolds-averaged Navier-Stokes (URANS).
- (9) Simulating film-cooling effectiveness using TFNS.

The numerical work was tied to an experimental campaign to measure the flow field and surface film effectiveness resulting from film cooling. Computations attempted to simulate and predict those experiments. The experimental campaign results are presented by Shyam et al. in Reference 8. In this report, the numerical work performed to achieve better agreement with the experimental data presented by Shyam et al. is described and evaluated in detail. The improved ability to simulate film-cooling flows is demonstrated and the need for additional refinements is discussed.

1.2 Experiment Setup and Conditions

A 30× engine scale test facility was used to interrogate the highly complex three-dimensional flow field associated with detached flows to resolve the shear layer and wake regions. A schematic of the test flow and geometry are shown in Figure 1. Experiments were carried out in an open-loop tunnel with a temperature-controlled coolant loop. The tunnel consisted of an aluminum bellmouth, flow-conditioning screens, 8.2-in.- (20.82-cm-) wide by 0.75 in.- (1.91-cm-) thick square acrylic sections, the test section on the tunnel floor, and a lid directly above for either viewing or actuator support. Air was drawn from the room and passed through flow-conditioning sections prior to the test section entry.

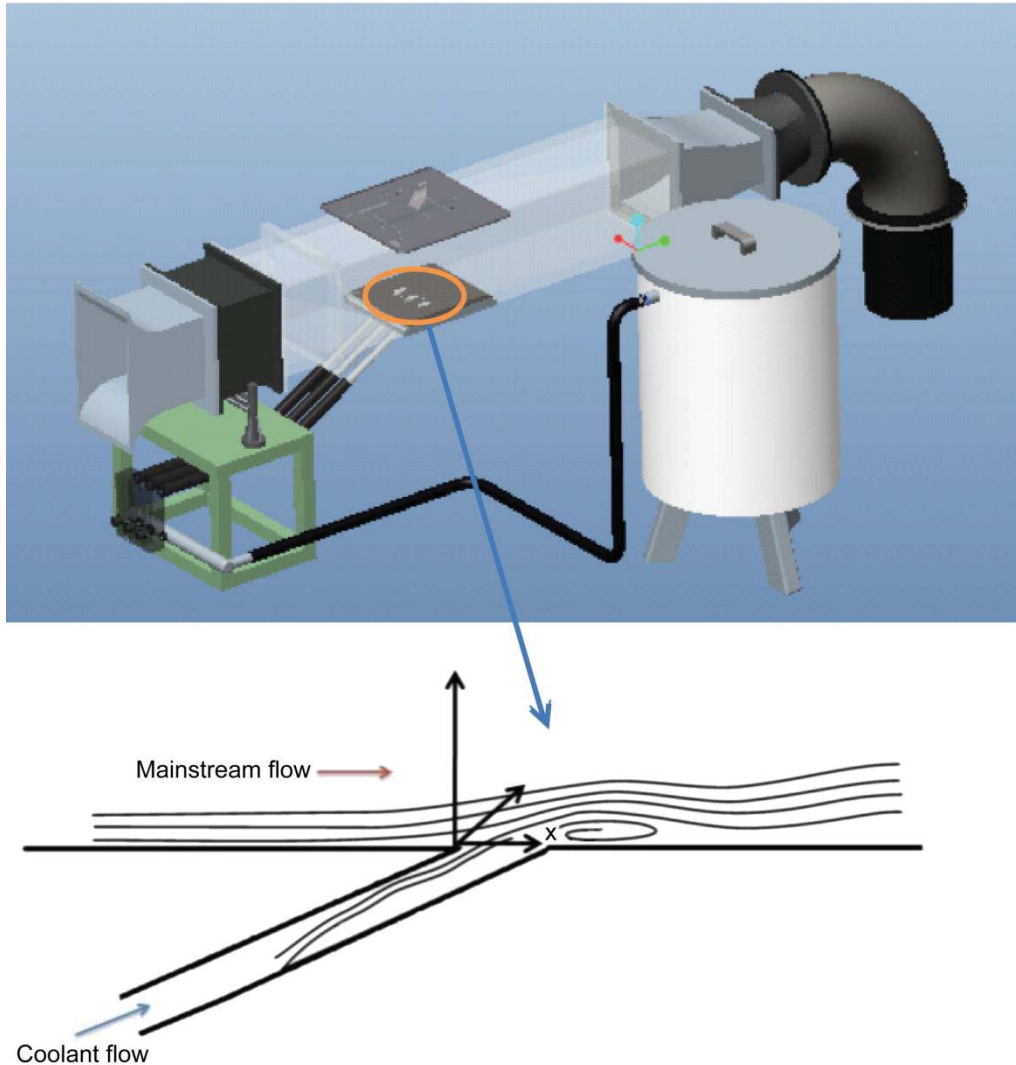


Figure 1.—Schematic of the tunnel setup and the cooling airflow with the long pipes (from Ref. 8).

Airflow was provided by a 7-hp (5220-W) fan. The free-stream velocity was 29.86 ft/s (9.1 m/s) and the Reynolds number was 11 000, based on free-stream velocity and coolant hole diameter (d). The test section is a square section of cross section measuring 8.00 by 8.00 in. (20.32 by 20.32 cm) by 34.00 in. (86.36 cm) in length (L). The free-stream turbulence intensity (Tu) at the inlet of the test section measured approximately 1.5 percent without a grid and 4 percent with a square grid (not used in the simulations). The boundary layer thickness was 1.27 cm at $x/d = -0.5$, and was taken to be the vertical distance from the wall at which the velocity is equal to 99 percent of the free-stream velocity.

Pressurized supply air provided coolant flow through a heat exchanger that consisted of a copper tube coiled inside in an ice water tank. The coolant was fed through a manifold to three separate flow meters then to acrylic tubes with $L/d = 20$ connected to each cooling hole. The separate cooling tubes provided an opportunity to model the cooling flow in each hole as fully developed.

The test section consisted of a flat acrylic plate with three 0.75-in.- (1.9-cm-) diameter holes inclined at 30°. The holes were spaced at three times the hole diameter.

To determine the tunnel flow rate, a total pressure probe was placed upstream of the test section and static pressure taps were placed on the sidewalls. Free-stream temperature was measured with an open-ball thermocouple located upstream of the holes near the total pressure probe. Coolant temperature was measured with open-ball thermocouples inside the coolant tubes. Temperature survey data was taken

along the centerline plane of the tunnel and at several cross sectional planes with a small open ball type E thermocouple probe attached to an actuator above the test section. The adiabatic wall temperature was determined from the thermocouple probe surveys with the probe located near the floor of the test section. Various hotwire probes were used to obtain the three-dimensional velocity components and turbulent stresses along the centerline and at several streamwise planes.

Infrared (IR) thermography was used to obtain the adiabatic film-cooling effectiveness. Further details and extensive data may be found in Shyam et al. (Ref. 8).

1.3 Time-Filtered Navier-Stokes Analysis

The unsteady approach called time-filtered Navier-Stokes (TFNS), also referred to as “partially resolved Navier-Stokes (PRNS) or very large eddy simulations” (Refs. 9 to 13), was used for this work. The method was developed for the simulation of large turbulent eddies and requires only relatively coarse grid resolution as is often used in RANS simulations. The method is based on the concept of temporal filtering of Navier-Stokes equations. This purportedly avoids grid dependence issues associated with LES such as the direct connection between the filter size and the grid resolution. In TFNS the larger timescales (or lower frequencies) of the turbulence are directly calculated and the effects of the unresolved turbulence timescales are modeled by a dynamic equation system. Contents of both resolved and unresolved turbulence are regulated by a filtering control parameter (FCP), which is related to the width of the temporal filter. The method as utilized in this work solves the flow all the way to the wall and avoids the use of wall functions.

The basic TFNS equations and its subfilter model presented by Liu and Shih (Ref. 9) are grid invariant, that is, they do not have grid spacing as a parameter in their formulations. It is therefore possible to achieve a grid-independent numerical solution for a fixed FCP. Another distinction is that TFNS enables performance of URANS, very large eddy simulations (VLES), LES, and even Direct Numerical Simulations (DNS) in a unified way through the judicious selection of the value of FCP, and the appropriately refined grid. It should be noted that the TFNS approach is not a variant of the hybrid RANS/LES (Refs. 16 to 19). There is no enforced transition between the perceived RANS and LES domains.

The subfilter model was constructed to use a more general relationship between the unresolved turbulent stresses and the resolved turbulent flow field. Shih and Liu (Ref. 11) used rational mechanics analysis and obtained a general constitutive relationship for the Reynolds stresses. In addition to the dissipative and diffusive effects accounted for through the eddy viscosity, the subfilter model accounts for the effects of anisotropy and rotation. Source terms introduced in the momentum equation sustain the turbulent fluctuations in the calculated flow field. One important outcome using this constitutive relationship described by Shih and Liu (Ref. 20) is the ability of TFNS to sustain turbulent fluctuations for a turbulent pipe flow in the lower range of applicable Reynolds numbers while the k - ϵ variant was not able to sustain a turbulent flow contrary to the observed physical behavior. The model adopted for TFNS simulations in the Glenn-HT code employs this unique feature of the nonlinear subfilter model.

A detailed description of the TFNS equations and the subfilter model developed by Shih and Liu (Ref. 11) follows in the next section.

1.3.1 Formulation

The formulation follows steps described in Reference 9. The additional formulation needed to implement the model without the use of wall functions is summarized from the literature and will be provided below.

Using a homogeneous temporal filter $G(t - t')$, the large timescale turbulence variable $\bar{\phi}$ and its density-weighted variable $\tilde{\phi}$ can be defined as

$$\bar{\phi}(t, x_i) = \int \phi(t', x_i) G(t-t') dt', \quad \tilde{\phi} = \frac{\bar{\rho}\phi}{\bar{\rho}} \quad (1)$$

where the integral is over the entire time domain and G satisfies the normalization condition $\int G(t-t') dt' = 1$.

There are several such temporal filters available, the simplest one is the top hat filter:

$$G(t-t') = \begin{cases} 1/\Delta_T, & \text{if } |t-t'| \leq \Delta_T/2 \\ 0, & \text{otherwise} \end{cases} \quad (2)$$

where Δ_T is the width of the top hat filter. Using this filter, the left part of Equation (1) becomes

$$\bar{\phi}(t, x_i) = \frac{1}{\Delta_T} \int_{t-\Delta_T/2}^{t+\Delta_T/2} \phi(t', x_i) dt' \quad (3)$$

Equation (3) suggests that $\bar{\phi}$ and $\tilde{\phi}$ become the exact Reynolds-averaged quantity and Favre-averaged quantity, respectively when $\Delta_T \rightarrow \infty$. On the contrary, they will become the instantaneous turbulent quantity as $\Delta_T \rightarrow 0$. For a finite Δ_T , they represent the quantities of large timescale turbulence.

Performing the filtering operation defined by Equation (1) on the Navier-Stokes equations, a set of exact, basic equations for the resolved, large timescale turbulence ($\bar{\phi}$ and $\tilde{\phi}$) are obtained:

$$(\bar{\rho}\tilde{u}_i)_{,t} + (\bar{\rho}\tilde{u}_i\tilde{u}_j)_{,j} = -\bar{p}_{,i} - \tau_{ij,j} + \left(2\bar{\mu}\tilde{s}_{ij} - \frac{2}{3}\delta_{ij}\bar{\mu}\tilde{s}_{kk} \right)_{,j} \quad (4)$$

$$(\bar{\rho}\tilde{e})_{,t} + (\bar{\rho}\tilde{u}_i\tilde{e})_{,i} = (\bar{\kappa}\tilde{T}_{,i})_{,i} + \overline{ps_{kk}} - q_{i,i} + \left(2\bar{\mu}s_{ij}s_{ij} - \frac{2}{3}\bar{\mu}s_{kk}s_{ii} \right) + \bar{Q} \quad (5)$$

$$\bar{\rho}_{,t} + (\bar{\rho}\tilde{u}_i)_{,i} = 0, \quad \bar{p} = \bar{\rho}R\tilde{T} \quad (6)$$

$$\tau_{ij} \equiv \bar{\rho}(u_i u_j - \tilde{u}_i \tilde{u}_j), \quad q_i \equiv \bar{\rho}(u_i e - \tilde{u}_i \tilde{e}) \quad (7)$$

where $s_{ij} = (u_{ij} + u_{ji})/2$. The operators $(\dots)_{,t}$ and $(\dots)_{,i}$ represent the temporal and spatial derivatives, respectively. The density, velocity, temperature, pressure, internal energy per unit mass, and the heating rate are represented by ρ , u_i , T , p , e , and Q , respectively. The viscosity and kinematic viscosity are given by μ and ν , κ is the heat conductivity of the fluid, and R is the universal gas constant. The extra terms created by the process of time-filtering nonlinear Navier-Stokes equations, τ_{ij} and q_i represent the effects of unresolved, small time-scale turbulence—the unresolved turbulent stresses and heat fluxes. The following was proposed to model the unresolved turbulent stresses τ_{ij} :

$$\begin{aligned} \tau_{ij} = & -2f_1\mu_T \left(\tilde{s}_{ij} - \delta_{ij}\tilde{s}_{kk}/3 \right) + \frac{1}{3}\delta_{ij}\tau_{kk} - A_3 f_3 \bar{\rho} \frac{k^3}{\epsilon^2} \left(\tilde{s}_{ik}\tilde{\omega}_{kj} - \tilde{\omega}_{ik}\tilde{s}_{kj} \right) \\ & + 2A_5 f_5 \bar{\rho} \frac{k^4}{\epsilon^3} \left[\tilde{\omega}_{ik}\tilde{s}_{kj}^2 - \tilde{s}_{ik}^2\tilde{\omega}_{kj} + \tilde{\omega}_{ik}\tilde{s}_{km}\tilde{\omega}_{mj} - \tilde{\omega}_{kl}\tilde{s}_{lm}\tilde{\omega}_{mk}\delta_{ij} + II_s \left(\tilde{s}_{ij} - \delta_{ij}\tilde{s}_{kk}/3 \right) \right] \end{aligned} \quad (8)$$

where k and ε are the turbulence kinetic energy and dissipation rate defined in Equations (17) and (18) $\tilde{s}_{ij} = (\tilde{u}_{i,j} + \tilde{u}_{j,i})/2$, $\tilde{\omega}_{ij} = (\tilde{u}_{i,j} - \tilde{u}_{j,i})/2$, $II_s = (\tilde{s}_{kk}\tilde{s}_{mm} - \tilde{s}_{kl}\tilde{s}_{lk})/2$. The model coefficients C_μ , A_3 , and A_5 are constrained by the realizability condition and the rapid distortion theory limit. They are not arbitrary but formulated in Reference 21:

$$C_\mu = \frac{1}{4.0 + A_s \frac{k}{\varepsilon} U^*}, \quad A_3 = \frac{\sqrt{1.0 - A_s^2 C_\mu^2 \left(\frac{k}{\varepsilon} S^*\right)^2}}{0.5 + 1.5 \frac{k^2}{\varepsilon^2} \Omega^* S^*}, \quad A_5 = \frac{1.6 \mu_T}{\bar{\rho} \frac{k^4}{\varepsilon^3} \frac{7 S^* S^* + \Omega^* \Omega^*}{4}} \quad (9)$$

in which

$$A_s = \sqrt{6} \cos \varphi, \quad \varphi = \frac{1}{3} \arccos(\sqrt{6} W^*), \quad W^* = \frac{S_{ij}^* S_{jk}^* S_{ki}^*}{(S^*)^3} \quad (10)$$

$$U^* = \sqrt{(S^*)^2 + (\Omega^*)^2}, \quad S^* = \sqrt{S_{ij}^* S_{ij}^*}, \quad \Omega^* = \sqrt{\omega_{ij} \omega_{ij}}, \quad S_{ij}^* = \tilde{s}_{ij} - \frac{1}{3} \delta_{ij} \tilde{s}_{kk} \quad (11)$$

Also,

$$\mu_T = \bar{\rho} C_\mu f_\mu \frac{k(k + \sqrt{\nu \varepsilon})}{\varepsilon} \quad (12)$$

The coefficients f_1 , f_3 , and f_5 are functions of Δ_T/T , that is, the ratio of the temporal filter width to the global timescale of the turbulent flow of interest, where the global timescale T can be considered as the maximum integral timescale in the entire domain. These functions must have the following property:

$$f_i \left(\frac{\Delta_T}{T} \right) = \begin{cases} 0 & \text{if } \frac{\Delta_T}{T} \rightarrow 0 \\ 1 & \text{if } \frac{\Delta_T}{T} \rightarrow 1 \end{cases} \quad (13)$$

This lets the unresolved turbulent stresses τ_{ij} vanish when the filter width Δ_T vanishes, and τ_{ij} approaches the Reynolds-averaged stresses as Δ_T increases towards the global timescale T .

All f_i have the same form in the TFNS model as

$$f_i \left(\frac{\Delta_T}{T} \right) \approx 2 \left(\frac{\Delta_T}{T} \right) - \left(\frac{\Delta_T}{T} \right)^2 \quad i = 1, 3, 5 \quad (14)$$

The ratio Δ_T/T is used to set the FCP. For example, $FCP = 0.30$, using $\Delta_T/T = 0.16$ is intending to directly resolve those turbulence scales that are responsible for about 70 percent of the total turbulent kinetic energy and model the rest of the unresolved turbulence scales that contain about 30 percent of the total turbulent kinetic energy. An FCP of 0.3 was used in these computations.

1.3.1.1 Modeling of Unresolved Turbulent Heat Fluxes

A common practice in modeling unresolved turbulent heat fluxes $q_i \equiv \bar{\rho} (u_i e - \tilde{u}_i \tilde{e})$ is to employ the following isotropic model:

$$q_i = -\kappa_T \tilde{e}_{,i} \quad (15)$$

The simplest form that considers the effects of strain and rotation should be

$$q_i = -\kappa_T \tilde{e}_{,i} - \kappa_T \frac{k}{\varepsilon} (c_1 \tilde{s}_{ij} + c_2 \tilde{\omega}_{ij}) \tilde{e}_{,j} \quad (16)$$

The expanded relationship resulted in unstable numerics and thus only one term was retained.

1.3.1.2 Transport Equations for Subscale k - ε

To complete the proposed model for τ_{ij} , k , and ε , the unresolved turbulent kinetic energy and its dissipation rate is needed. The exact transport equations can be derived from Navier-Stokes equations, and contain several higher order of unclosed terms due to the temporal filtering operation. The first step in the derivation procedure is to establish the transport equation for τ_{ij} , followed by a tracing operation to establish the equation for τ_{ii} (which is $\bar{\rho} k$), and this leads to the transport equation for k .

In the current implementation a low Reynolds number version of the equations is used to allow direct solution in the near-wall regions without the use of wall functions. The damping functions used are from References 21 and 22. The equations and the damping functions are as follows:

$$\frac{\partial}{\partial t} \bar{\rho} k + \frac{\partial}{\partial x_i} \bar{\rho} \tilde{u}_i k = \frac{\partial}{\partial x_i} \left[(\bar{\mu} + \mu_T) \frac{\partial k}{\partial x_i} \right] - \tau_{ij} \tilde{s}_{ij} - \bar{\rho} \varepsilon \quad (17)$$

A model transport equation for the dissipation rate ε was constructed by the analogy to Equation (17) as

$$\frac{\partial}{\partial t} \bar{\rho} \varepsilon + \frac{\partial}{\partial x_i} \bar{\rho} \tilde{u}_i \varepsilon = \frac{\partial}{\partial x_i} \left[(\bar{\mu} + \mu_T) \frac{\partial \varepsilon}{\partial x_i} \right] - C_{\varepsilon 1} f_{\varepsilon 1} \tau_{ij} \tilde{s}_{ij} \frac{\varepsilon}{k} - \frac{C_{\varepsilon 2} f_{\varepsilon 2} \bar{\rho} \varepsilon^2}{k + \sqrt{\nu \varepsilon}} + \frac{C_{\varepsilon 3} \bar{\mu} \mu_T}{\bar{\rho}} \tilde{s}_{,j} \tilde{s}_{,j} \quad (18)$$

where $C_{\varepsilon 1} = 1.45$, $C_{\varepsilon 2} = 1.92$, and $C_{\varepsilon 3} = 1.0$; while keeping in mind that they can be further constructed as functions of the local subscale turbulence quantities (Ref. 14):

$$f_{\mu} = 1 - \exp \left\{ \sum_{i=1}^5 a_i R^i \right\} \quad (19)$$

$$f_{\varepsilon 1} = 1 - \exp \left\{ - \sum_{i=1}^5 a'_i R^i \right\} \quad (20)$$

$$f_{\varepsilon 2} = 1 - 0.22 \exp(-R_t^2/36) \quad (21)$$

also
$$R = \frac{\sqrt{k}(k + \sqrt{\nu \varepsilon})^{3/2}}{\nu \varepsilon} \quad (22)$$

and

$$R_t = \frac{\rho k^2}{\mu \varepsilon} \quad (23)$$

The coefficients are given in Table I.

TABLE I.—COEFFICIENTS FOR EQUATIONS (19) AND (20)

	1	2	3	4	5
a_i	3.3×10^3	-6.0×10^{-5}	6.6×10^{-7}	-3.6×10^{-9}	8.4×10^{-12}
a'_i	2.53×10^{-3}	-5.7×10^{-5}	6.55×10^{-7}	-3.6×10^{-9}	8.3×10^{-12}

Low-Reynolds-number terms that do not use wall distance were deemed more appropriate for the class of flows of interest in this work, which involve separated boundary layers. Note the wall distance does not appear in the model terms.

2.0 Film-Cooling Flow Computations

The numerical scheme and the turbulence model were implemented in the Glenn-HT code (Ref. 15), a multiblock-structured grid N-S solver. The computer code uses a four-stage multistage Runge-Kutta scheme with fourth-order artificial dissipation with eigenvalue scaling. The added model, in its steady form, was applied to flow over a flat plate and the resulting wall friction and heat transfer from an adiabatic wall and a heated wall, respectively, were computed and found to be in good agreement with correlations.

Subsequent film-cooling flow computation simulations were conducted in accordance with experimental conditions. Geometric scaling was performed to raise the flow Mach number and to maintain the Reynolds number based on the film-cooling hole. The density ratio of the flow was held to near unity by adjusting the total temperature at the hole inlet. Even though blowing ratios of 0.5, 1.0, 1.5, and 2.0 were computed, only ratios of 0.5 and 1.0 are discussed in this report. The computational domain extended 12 diameters upstream and 16 diameters downstream of the cooling hole. Spacing between the holes was equal to three hole diameters in the experiment. For the computations, a period of 3 diameters was similarly imposed. However, it was understood that due to flow unsteadiness, imposition of periodicity is a simplification that is done to reduce computation resource requirements. The free-stream boundary condition was placed at five diameters from the wall where an exit boundary condition was specified. An exit boundary condition was also specified at the outlet on the domain.

The Tu (1.5 percent as measured) and a turbulence length scale were specified at the inlet. No particular handling of the inlet boundary condition to include unsteadiness for our TFNS computations was performed. Also, the grid upstream of the hole region was not as well refined as in the vicinity of the hole. This causes the incoming flow to be steady. Cases where the grid is refined in the inlet region and inclusion of unsteady boundary condition should be considered as a follow-on to this work. This will involve modifications to the inlet boundary condition briefly mentioned in this report.

A number of grid blocks were assigned to individual CPUs in a way that allowed balanced parallel computing. To reduce communications overhead, smaller blocks were further consolidated before implementing grouping. Initially, 120 groups (CPUs) were used by refining blocking. It was possible to increase that number to 1200 for improved parallel capability. The grid itself contained approximately 8 million cells. Particular attention was paid to grid refinement in areas near the no-slip walls and the cooling hole outlet and downstream of the cooling hole with wall shear-stress-scaled grid spacing of $\Delta x^+ < 300$, $\Delta y^+ < 3$, $\Delta z^+ < 200$. Grid cells in the film-cooling flow core were constructed to be uniform and nearly cubic in shape. Figure 2 shows the grid topology. Figure 2(a) shows the computational domain with multiple blocks; Figure 2(b), the grid along the symmetry plane; and Figure 2(c) and Figure 2(d), closeup views of the grid near the cooling hole.

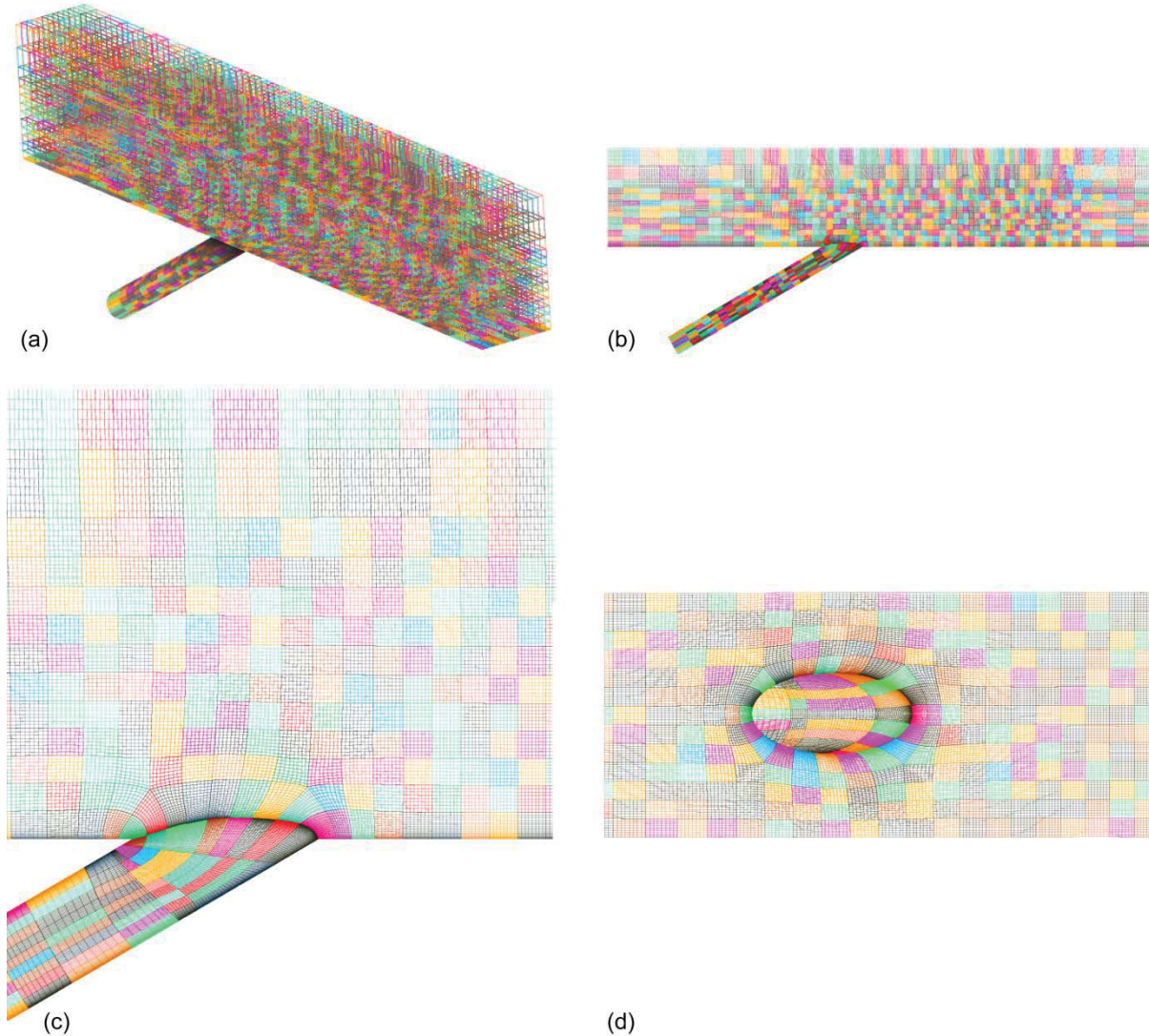


Figure 2.—Grid topology. (a) Computational domain with multiple blocks. (b) Grid along symmetry plane. (c) Closeup view of grid along symmetry plane near hole exit. (d) Top view of surface grid in hole.

2.1 RANS and URANS Analysis

As previously mentioned, film-cooling effectiveness prediction accuracy suffers greatly when RANS is used and the blowing ratio is relatively high ($> \sim 1$). RANS and URANS computations were performed to assess their performance in predicting the film-cooling effectiveness before TFNS computations were performed. Figure 3 shows the experimental measurements of the laterally averaged effectiveness of film cooling downstream of the hole and predictions using a variety of models available in Glenn-HT code and the commercial code. Computations were performed for a blowing ratio $M = 1$ and density ratio $DR = 1$. The effectiveness data were obtained using thermocouples and documented in Reference 8. Results were obtained on a once-coarsened version of the grid shown in Figure 2 using both RANS and URANS versions of the model described earlier. In addition, the low-Reynolds-number SST model developed by Langtry and Sjolander (Ref. 23) was used and implemented in the code for this work. For the runs with CFX commercial code, two turbulence models, namely, Menter's SST and the standard $k-\epsilon$ model were utilized (Ref. 24).

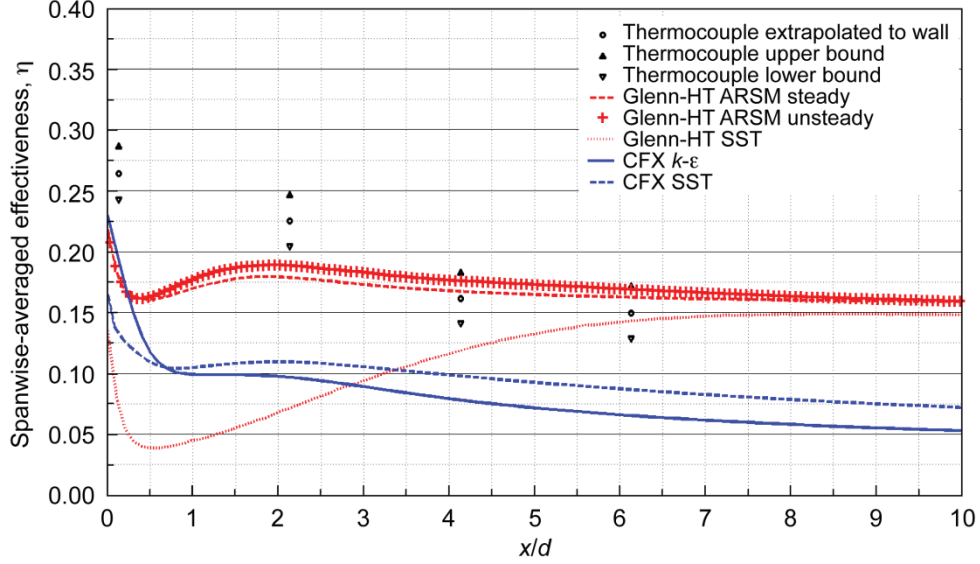


Figure 3.—Measured and computed laterally averaged effectiveness downstream of film-cooling holes.

Effectiveness is defined as one of the following:

$$\eta = (T_{\infty} - T_{aw}) / (T_{\infty} - T_c) \quad (24)$$

or

$$\eta_1 = (T_r - T_{aw}) / (T_r - T_c) \quad (25)$$

The results above are for η and show a large variance and dependence on the chosen turbulence models. T_{∞} refers to the inlet total temperature, T_{aw} is the adiabatic wall temperature, T_c is the coolant temperature, and T_r is the recovery temperature (adiabatic wall temperature) between the holes in a region not affected by film cooling as was the case in the experimental measurements.

2.2 TFNS Solutions

Two sets of computations using the TFNS method—a density ratio of unity ($DR = 1$) and the blowing ratios of 0.5 and 1.0—are presented in the following sections. As mentioned previously, the FCP for the TFNS was set to 0.3. The dimensionless time step was set to 0.005 and the CFL to 3.0 with residual smoothing turned on. Other important parameters for computations are the second- and fourth-order artificial dissipation terms coefficients used along with the second-order central scheme (Ref. 15). Those coefficients were $\kappa_2 = 0.125$ and $\kappa_4 = 0.001$. The value of the second-order dissipation was not critical as the flow was wholly subsonic, but a smaller value of the fourth-order dissipation coefficient of $\kappa_4 = 0.0005$ produced nonphysical wiggles in the solution and thus κ_4 was selected as the lowest safe value that produced smooth solutions.

2.2.1 Blowing Ratio of 0.5

Figure 4 plots spanwise-vorticity contours, which show the development of vortical structures downstream of the cooling hole. Shedding occurs because of coolant interaction with the mainstream flow. Tyagi and Acharya (Ref. 3) asserted that the observed vortical structures in film-cooling flow are related to the development, evolution, growth, and transport of the hairpin vortices.

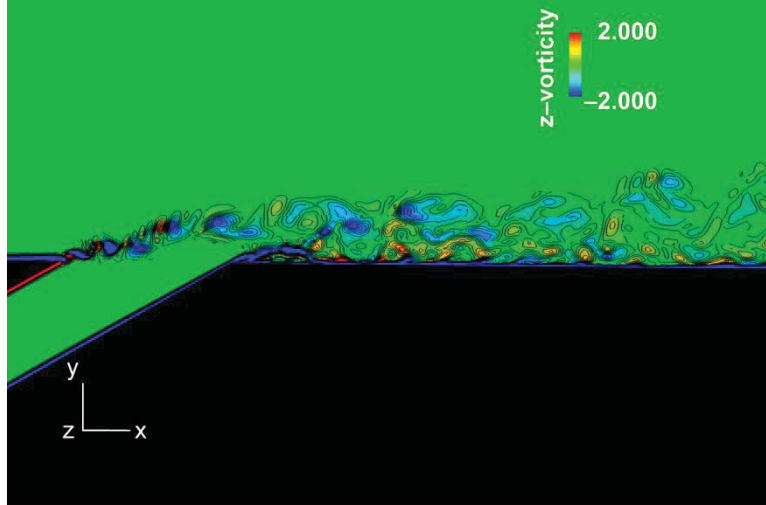


Figure 4.—Initiation of rib vortices and convection downstream.

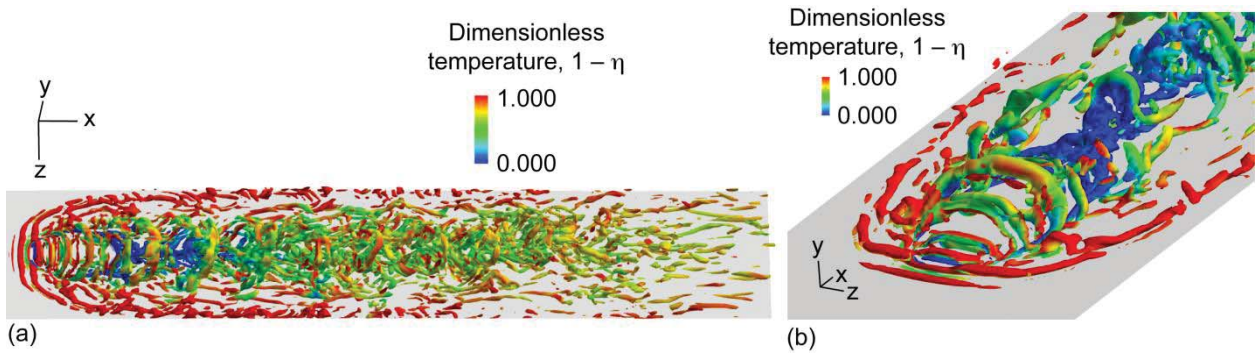


Figure 5.— Q -criterion isosurfaces of $Q^* = 0.1$ at $M = 0.5$ and $DR = 1.0$. (a) Overview of the domain. (b) Near-hole view.

Figure 5 shows isosurface presentation of the dimensionless quantity $Q^* = 0.1$, of the Q -criterion (Ref. 25) defined as $0.5 (\omega_i \omega_i - S_{ij} S_{ij})$ where the positive values represent locations in the flow where the vorticity dominates the strain. The isosurfaces are colored by the nondimensional temperature $1 - \eta$, thus the blue regions show cooling air and the red regions are at free-stream conditions. The cooling air with the higher density propagates downstream with periodic mixing patterns and appears first at a location slightly upstream of the hole and stays periodic some distance downstream before it starts to become random. The patterns indicate definite rib vortices that form around the film column and convect downstream. These ribs appear to be quite regular and are likely to be of the Kelvin-Helmholtz instability wave type. Hairpin vortices are seen further downstream of the rib vortices as shown in Figure 5. The coherent vortical structures persist for several hole diameters downstream of the hole and then break up. This may coincide with the rapid deterioration in effectiveness seen in Figure 6, particularly in the spanwise direction shown as a well-defined narrowing of the color bands.

Figure 7 shows the computed time-averaged film effectiveness contours for this case and the experimental measurements using IR thermography from Reference 8.

The differences between the distribution of the surface effectiveness generated by CFD and that produced by IR thermography may be attributable to an inconsistency between the measured (experimental) and computed upstream boundary conditions. A recent LES study by Ziefle and Kleiser (Ref. 26) discussed the effect of the unsteady cross-stream inlet condition on the cooling effectiveness. Figure 8 shows this difference clearly. According to Ziefle and Kleiser, effectiveness contours produced

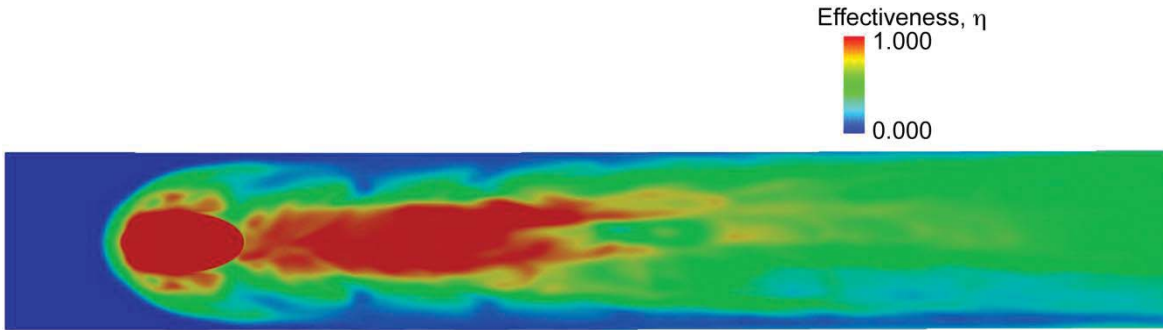


Figure 6.—Computed instantaneous effectiveness contours for $M = 0.5$ and $DR = 1.0$.

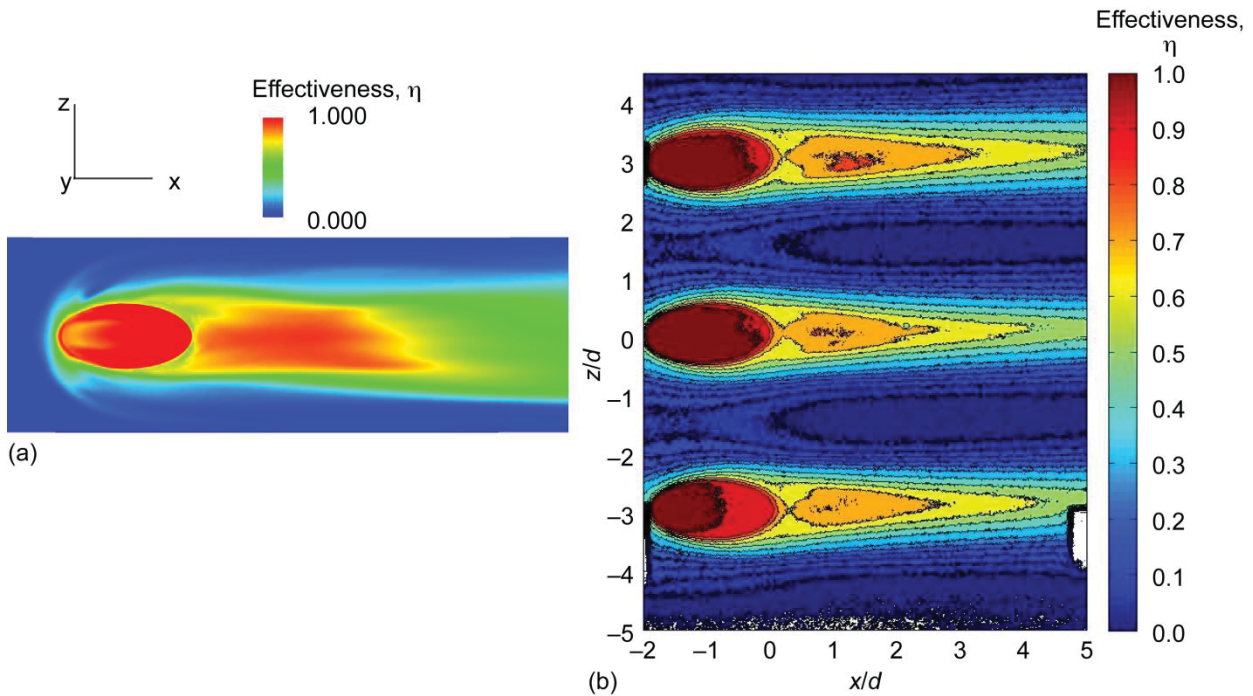


Figure 7.—Time-averaged film effectiveness contours for $M = 0.5$ and $DR = 1.0$. (a) Computed. (b) Experimental (from Ref. 8).

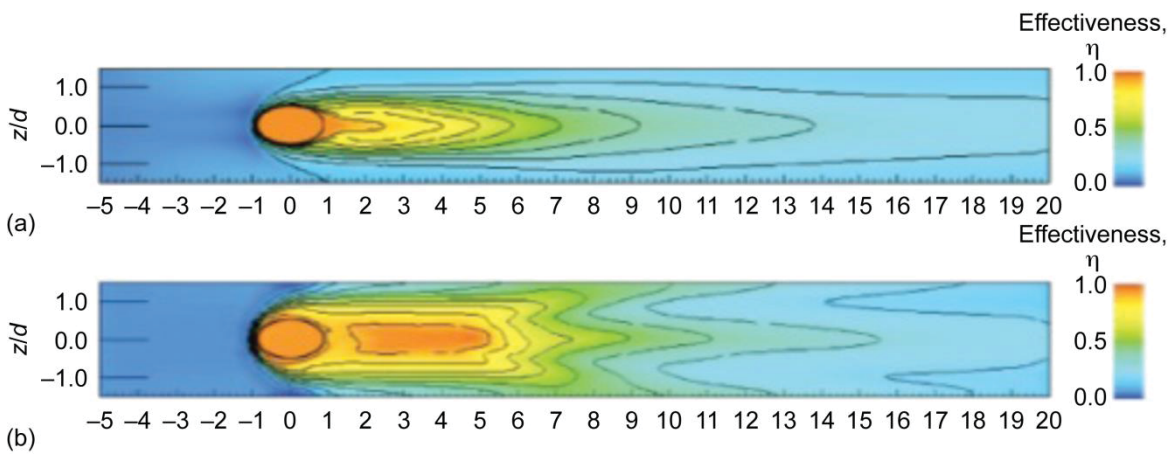


Figure 8.—Comparison of the film effectiveness η contour distributions (from Ref. 26). (a) With unsteady cross stream. (b) Without unsteady cross stream.

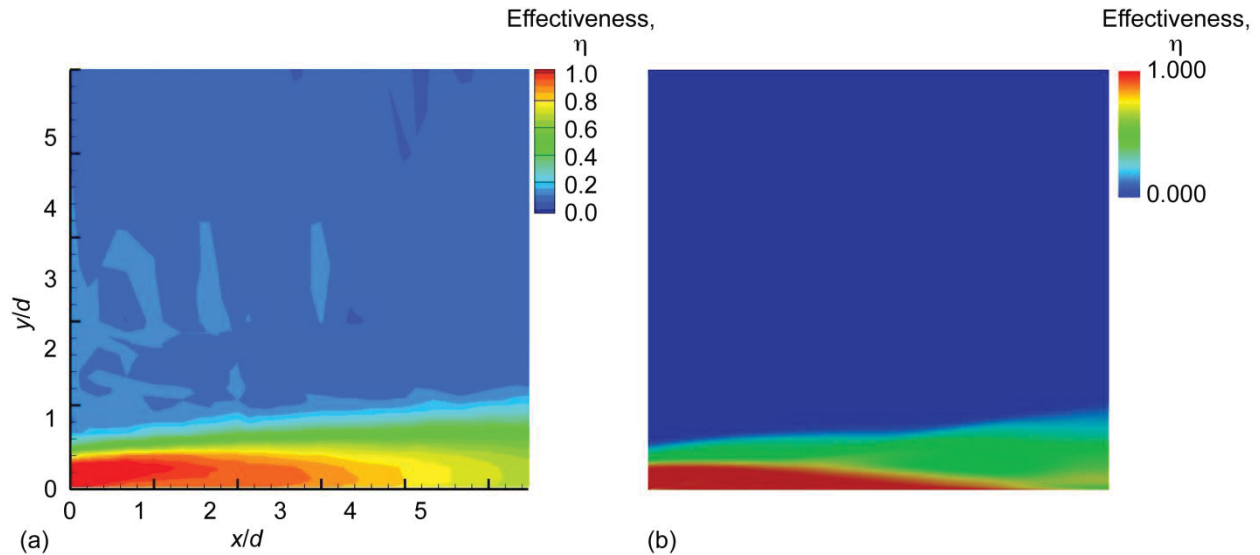


Figure 9.—Centerline film effectiveness contours for $M = 0.5$ and $DR = 1.0$. (a) Measured. (b) Computed.

by their own LES computations were three tailed, similar to Figure 7(a), when steady crossflow was established upstream (Figure 8(a)), as is the case with our TFNS computations. Contours were pointed in the downstream direction (Figure 8(b)) when realistic unsteady crossflow was set up upstream. As described earlier, the experimental measurements of effectiveness were made with an unsteady upstream condition characterized by a Tu of 1.5 percent. Therefore suitable unsteady inlet boundary condition is needed to allow for simulation of realistic film-cooling flows and to be able to directly compare to the experimental data in Reference 8. Johnson and Shyam (Ref. 27) used a recycling and rescaling method to model a more realistic inlet boundary to the film-cooling jet and they saw some improvement to the physical structures but not a significant improvement in effectiveness prediction. A more effective approach to obtaining improved simulations could be the synthetic eddy modeling (SEM) devised by Jarrin et al. (Ref. 28) applied to the mainstream flow.

Figure 9(a) shows the measured dimensionless quantity of film effectiveness along the center plane of the film-cooling hole, and Figure 9(b) shows the computed contour lines for the same domain. The measured quantities were taken using thermocouples (Ref. 8). The computational contours of effectiveness (η_1) are not as diffused as the measured ones. Note that the values of effectiveness calculated from the thermocouple data do not approach zero above the jet in the free stream while the computed results in Figure 9(b) did as expected. Effectiveness is based on tunnel inlet total temperature as shown in Equation (22), and is zero upstream of the hole. Correcting for that discrepancy enhances the agreement with the experimental data but the main discrepancy appears to be caused by not accounting for the crossflow unsteadiness in the computations. Ziefle and Kleiser show the effect of the crossflow unsteadiness. Figure 10(a) shows the contours of effectiveness in the presence of crossflow unsteadiness while Figure 10(b) shows the contours in the absence of such unsteadiness. It is clear that the cross-stream turbulence enhances breakup of the cooling jet and promotes its dissipation. The differences between the measurements in Figure 9(a) and computations in Figure 9(b) are likely similarly attributable to the effect of the crossflow unsteadiness.

Figure 11 and Figure 12 show the respective spanwise-averaged and the centerline values of film-cooling effectiveness for $M = 0.5$ and $DR = 1.0$. The green line shows effectiveness from IR thermography for a case with higher Tu (4 percent). The results from IR thermography for low turbulence are within the error bands of the thermocouple data. Spanwise-averaged effectiveness (η_1), plotted as the red line in Figure 11, appears to overpredict the measured data. The discussion by Ziefle and Kleiser on the effect of

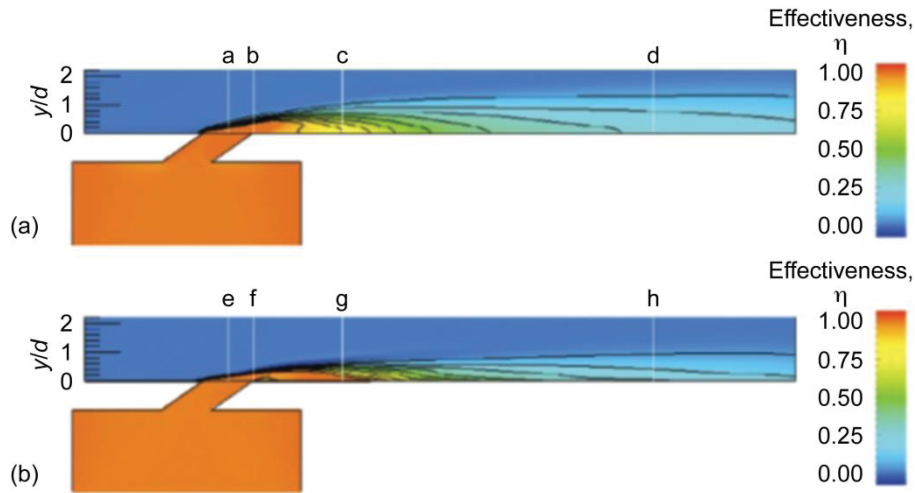


Figure 10.—Film effectiveness contours through the centerline of the film-cooling hole from Reference 26. (a) With unsteady cross stream. (b) Without unsteady cross stream.

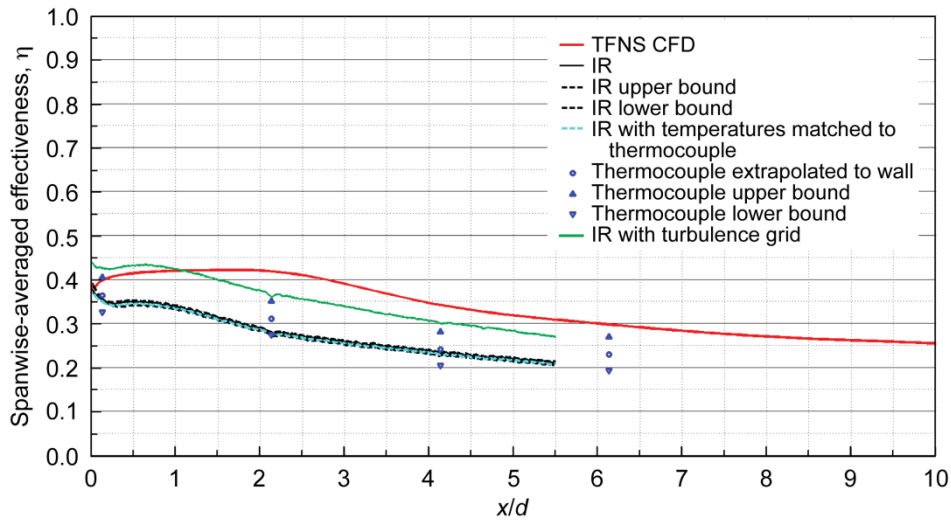


Figure 11.—Spanwise-averaged film effectiveness for $M = 0.5$ and $DR = 1.0$.

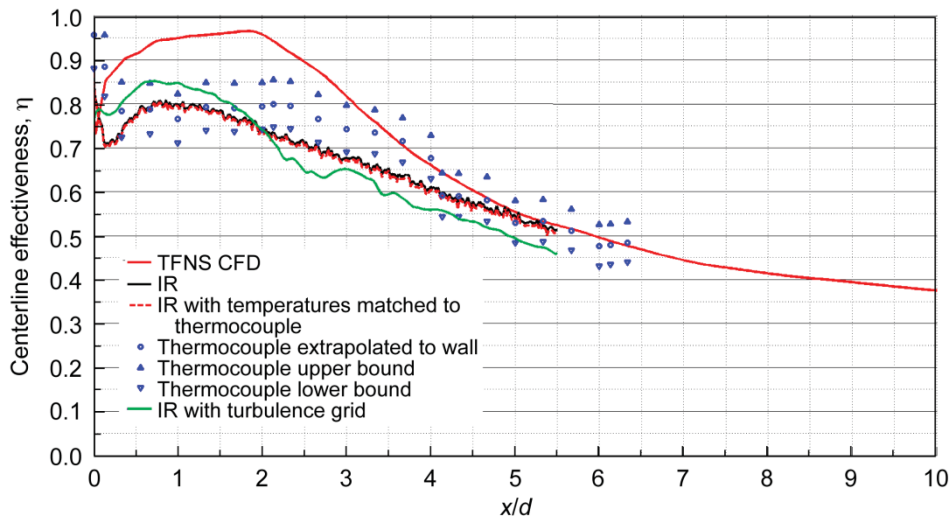


Figure 12.—Centerline film effectiveness for $M = 0.5$ and $DR = 1.0$.

the neglected cross-stream unsteadiness applies here. In addition, LES computations performed by Tyagi and Acharya for the blowing ratio of 0.5 for the 35° short hole pipe, produced high effectiveness similar to what is shown in Figure 11. Tyagi and Acharya applied random fluctuations using a Gaussian distribution with its variance taken from the kinetic energy of turbulence. Thus no coherence existed in the incoming flow. This type of specification dies out rapidly and does not result in unsteady free stream. This similarity suggests that the presence of an unsteady inlet boundary condition may be crucial to agreement with the experimental data. Note that the CFD results show that a relatively high level of cooling effectiveness is maintained much further downstream of the hole than the experiment, and is consistent with the contours shown in Figure 9.

2.2.2 Blowing Ratio of 1.0

Figure 13 shows isosurfaces of the Q^* for the case of $M = 1$ and $DR = 1$. The level of Q^* was held at 0.1 to allow for comparison with the $M = 0.5$ computation. The horseshoe vortex appears to have been initiated at the leading edge of the cooling hole. Figure 13(a) shows a better formed horseshoe vortex compared to the $M = 0.5$ case. The initial mixing region between the two streams seems to have more of an axial vorticity character than the previous case where it had more of the ring-type character. Ring vortices are also present in the near-hole region, and the rings and vortex filaments show a higher level of mixing than previously observed for the lower blowing case. The ring vortices appear to be organized, survive for some distance, and dissipate toward the end of the domain.

Figure 14(a) shows cooling effectiveness contours on the plate surface from IR thermography for a free-stream Tu of 1.5 percent. The maximum effectiveness downstream of the hole is approximately 0.45 and occurs at approximately 2.5 diameters downstream of the hole trailing edge. In addition, the contours appear to be aligned with the flow direction indicating that there is uniform cooling that seems to extend downstream and does not drop off as quickly as for $M = 0.5$. The coverage appears to extend to $y/d = \pm 1$ and the coverage shown by the CFD results in Figure 14(b) is narrower than the experimental data. The difference between experimental and computed contours is most pronounced near the hole. The low values of effectiveness downstream of the hole in Figure 14(b) are due to a lack of mixing of the free stream and the cooling flows, and is an indication of jet lift-off. Again, for this case, absence of unsteadiness in the free stream is a likely reason for the differences in effectiveness.

Figure 15 shows the local effectiveness at a plane located at $z/d = 0.0$ based on thermocouple surveys. Notice in the region between $x/d = 0.5$ to 2.0 an area of relatively lower effectiveness appears. The computed contours, while showing similar behavior, have a wider lift-off zone and narrower height of the jet as they protrude into the free stream. This can be attributed to the neglected effect of the unsteady cross stream discussed in relation to Figure 9 and Figure 10.

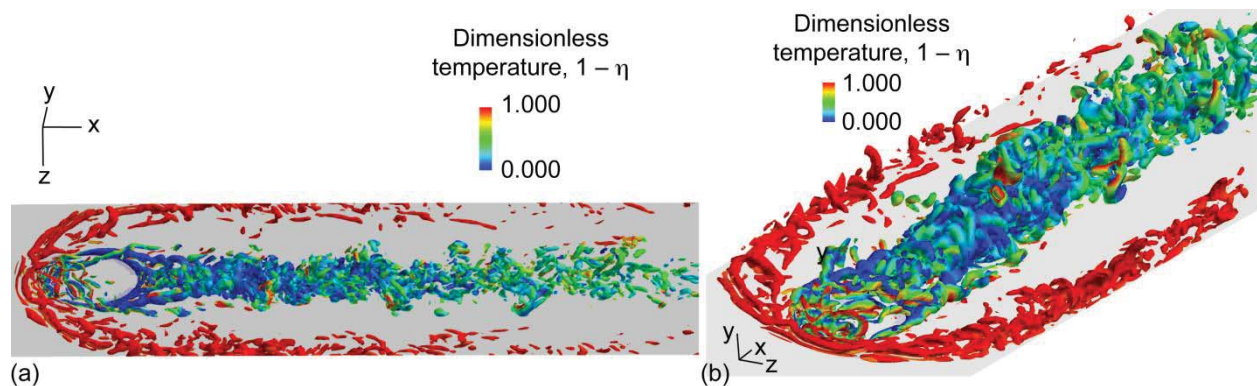


Figure 13.— Q -criterion isosurfaces of $Q^* = 0.1$ at $M = 1.0$ and $DR = 1.0$. (a) Overview of the domain. (b) Near-hole view.

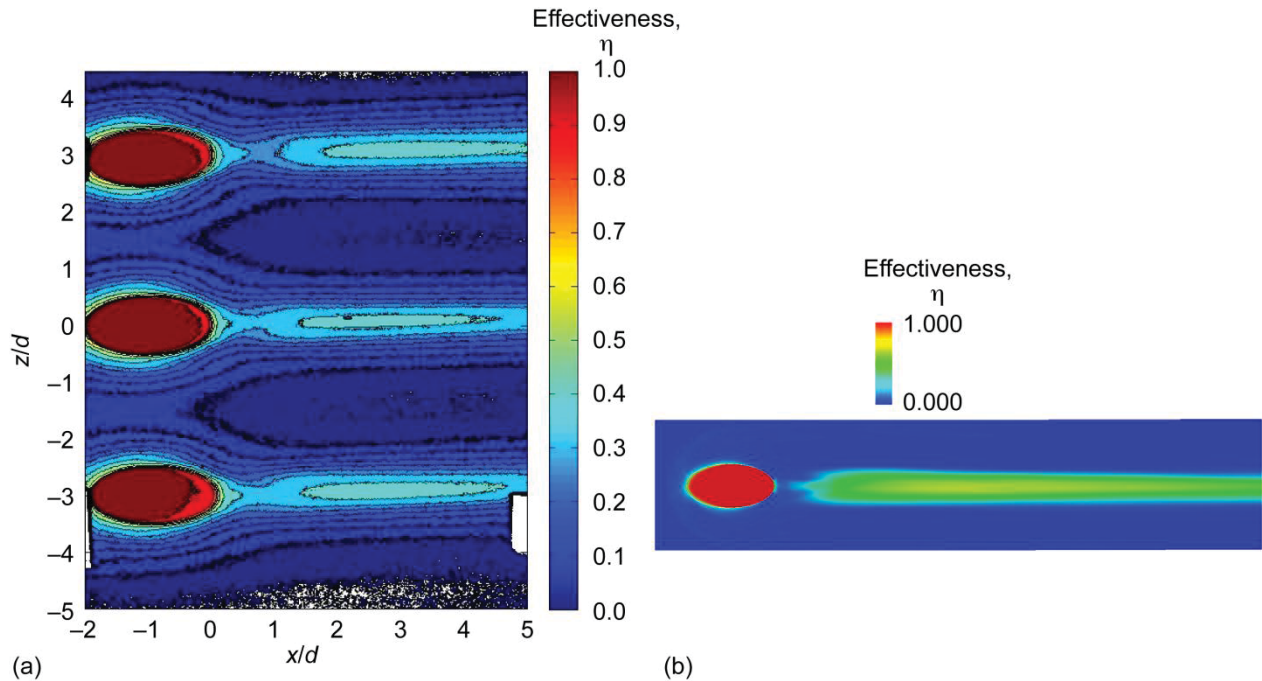


Figure 14.—Film-cooling effectiveness contours downstream of hole for $M = 1.0$, $DR = 1.0$, and $Tu = 1.5$ percent. (a) Measured. (b) Computed.

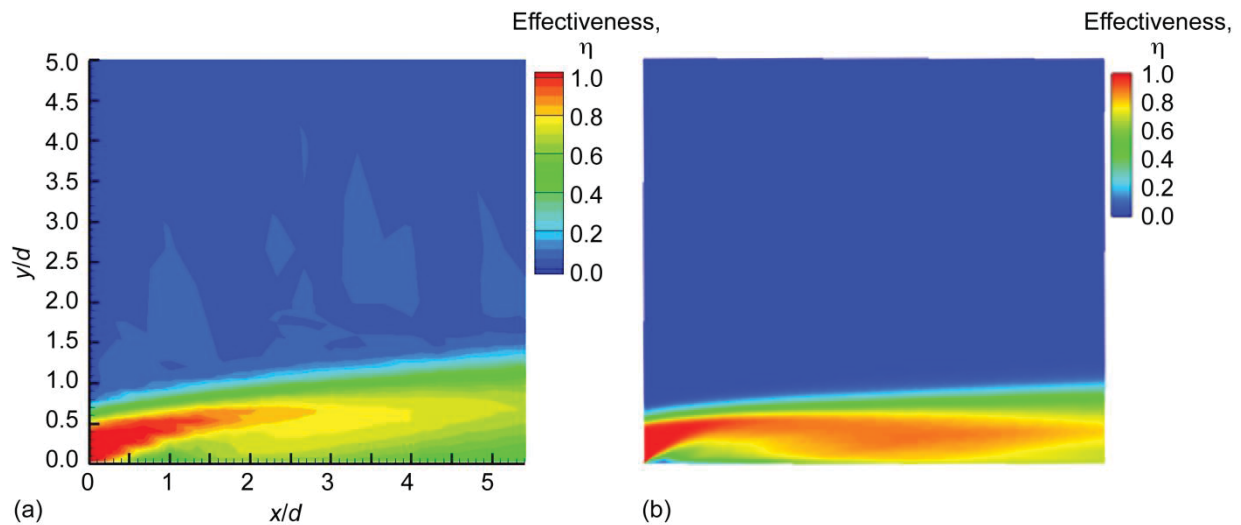


Figure 15.—Centerline film effectiveness contours at $M = 1.0$ and $DR = 1.0$. (a) From thermocouple survey $Tu = 1.5$ percent (b) Computed contours.

Figure 16 and Figure 17 show spanwise-averaged and centerline effectiveness for $M = 1.0$, $DR = 1.0$, and $Tu = 1.5$. Computed results start out with a dropoff in the span-averaged effectiveness from excessive jet lift-off as shown in Figure 16. Jet reattachment, not seen in the experiment, causes a rise in the centerline effectiveness (Figure 17). This is one of the most important phenomena in the simulation of film cooling and is resolved by including the effect of inlet unsteadiness into simulations.

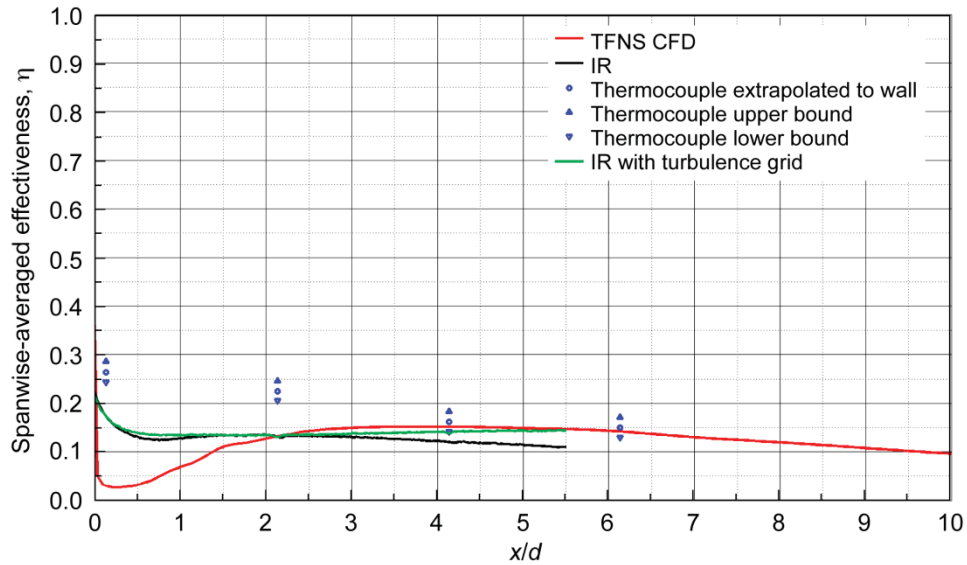


Figure 16.—Spanwise-averaged film effectiveness for $M = 1.0$, $DR = 1.0$, and $Tu = 1.5$.

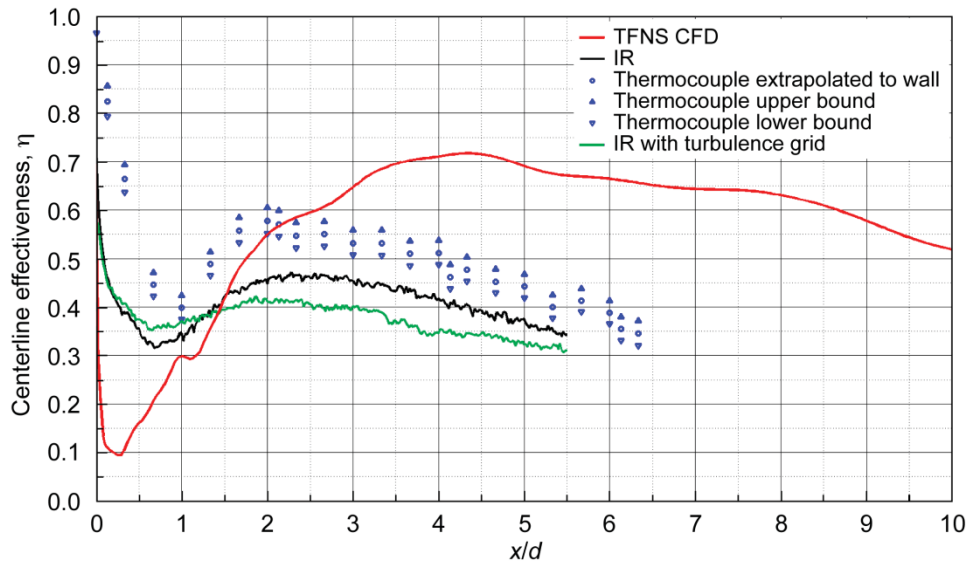


Figure 17.—Centerline film effectiveness for $M = 1.0$, $DR = 1.0$, and $Tu = 1.5$.

3-Conclusions

The time-filtered Navier-Stokes (TFNS) method was implemented in the Glenn-Heat Transfer (Glenn-HT) code and analyses of a flat plate cooled by long holes inclined at 30° to the free stream were conducted to obtain both steady and unsteady flow solutions. The data were provided by an accompanying experiment. Results showed that steady solutions are highly dependent on the turbulence model used. To reduce this dependence, the unsteady TFNS analysis was used. The purpose is to allow resolution of larger unsteady flow structures believed to be mainly responsible for the breakup of the film-cooling stream. Features such as Kelvin Helmholtz structures resulting from the interaction of the two streams and vortical structures associated with hairpin vortices can be observed in the simulated flows.

Good agreement was not achieved when the film effectiveness distributions obtained from the computations were compared to the experimental IR thermography. Based on the literature for the blowing ratio of 0.5, it was concluded that achieving a successful agreement between the computational

results and the experimental data requires matching of the free-stream turbulence, which the Glenn-HT code is not equipped to do at this time. Results of the TFNS computations, however, are consistent with computations performed in the literature without the effect of free stream.

References

1. El-Gabry, L.; Heidmann, J.; and Ameri, A.A.: Numerical Analysis of Film Cooling at High Blowing Ratio. NASA/TM—2009-215517, 2009. <http://ntrs.nasa.gov>
2. Guo, X.; Schröder, W.; and Meinke, M.: Large-Eddy Simulations of Film Cooling Flows. *Comput. Fluids*, vol. 35, 2006, pp. 587–606.
3. Tyagi, M.; and Acharya, S.: Large Eddy Simulation of Film Cooling Flow From an Inclined Cylindrical Jet. *Trans. ASME, J. Turbomach.*, vol. 125, 2003, pp. 734–742.
4. Fujimoto, S.: Large Eddy Simulation of Film Cooling Flows Using Octree Hexahedral Meshes. GT2012–70090, 2012.
5. Sinha, A.K.; Bogard, D.G.; and Crawford, M.E.: Film-Cooling Effectiveness Downstream of a Single Row of Holes With Variable Density Ratio. *Trans. ASME, J. Turbomach.*, vol. 113, 1991, pp. 442–449.
6. Martini, P., et al.: Detached Eddy Simulation of Film Cooling Performance on the Trailing Edge Cutback of Gas Turbine Airfoils. *Trans. ASME, J. Turbomach.*, vol. 128, no. 2, 2006, pp. 292–299.
7. Peet, Y.; and Lele, S.K.: Computational Framework for Coupling Compressible and Low Mach Number Codes. *AIAA J.*, vol. 46, no. 8, 2008, pp. 1990–2001.
8. Shyam, V., et al.: Long Hole Film Cooling Dataset for CFD Development, Part 1: Infrared Thermography and Thermocouple Surveys. NASA/TM—2013-218086-PART1, 2013. <http://ntrs.nasa.gov>
9. Liu, N.-S.; and Shih, T.-H.: Turbulence Modeling for Very Large-Eddy Simulation. *AIAA J.*, vol. 44, no. 4, 2006, pp. 687–697.
10. Shih, T.-H.; and Liu, N.-S.: Modeling of Internal Reacting Flows and External Static Stall Flows Using RANS and PRNS. *Flow, Turbulence and Combustion*, vol. 81, 2008, pp. 279–299.
11. Shih, T.H.; and Liu, N.S.: A Nonlinear Dynamic Subscale Model for PRNS/VLES of Internal Combustor Flows. AIAA–2009–0467, 2009.
12. Liu, Nan-Suey; Wey, Thomas; and Shih, Tsan-Hsing: Time-Filtered Navier-Stokes Approach and Emulation of Turbulence-Chemistry Interaction. AIAA 2013–0707, 2013.
13. Shih, Tsan-Hsing, et al.: Modeling of Turbulent Swirling Flows. NASA TM–113112, 1997. <http://ntrs.nasa.gov>
14. Wilcox, D.C.: Simulation of Transition With a Two-Equation Turbulence Model. *AIAA J.*, vol. 32, no. 2, 1994, pp. 274–255.
15. Steinthorsson, E.; Liou, M.S.; and Povinelli, L.A.: Development of an Explicit Multiblock/Multigrid Flow Solver for Viscous Flows in Complex Geometries. AIAA–93–2380 (NASA TM–106356), 1993.
16. Davidson, L.; and Peng, S.H.: Hybrid LES–RANS Modeling: A One-Equation SGS Model Combined With a κ – ω Model for Predicting Recirculating Flows. *Int. J. Numer. Meth. Fl.*, vol. 43, 2003, pp. 1003–1018.
17. Larsson, J.; Lien, F.S.; and Yee, E.: The Artificial Buffer Layer and the Effect of Forcing in Hybrid LES/RANS. *Internat. J. Heat Fluid Flow*, vol. 28, 2007, pp. 1443–1459.
18. Spalart, P.R.; Jou, W.H.; and Allmaras, S.R.: Comments on the Feasibility of LES for Wings and on a Hybrid RANS/LES Approach. *Advances in DNS/LES*, Greyden Press, Dayton, OH, 1997.
19. Fasel, H.F.; von Terzi, D.A.; and Sandberg, R.D.: A Methodology for Simulating Compressible Turbulent Flows. *J. App. Mech.*, vol. 73, pp. 405–412.
20. Shih, Tsan-Hsing; and Liu, Nan-Suey: Assessment of a Partially Resolved Numerical Simulation (PRNS) Approach in the National Combustor Code (NCC) for Turbulent Non-Reacting and Reacting Flows. NASA/TM—2008-215418, 2008. <http://ntrs.nasa.gov>
21. Shih, Tsan-Hsing, et al.: Modeling of Turbulent Swirling Flows. NASA TM–113112, 1997. <http://ntrs.nasa.gov>
22. Shih, T-S; Chen, K-H; and Liu N-S: A Non-Linear k – ε Model for Turbulent Shear Flows. AIAA 98–3983, 1998.

23. Langtry, R.B.; and Sjolander, S.A.: Prediction of Transition for Attached and Separated Shear Layers in Turbomachinery. AIAA 2002-3641, 2002.
24. ANSYS CFX Reference Guide. Release 13, 2010.
http://www1.ansys.com/customer/content/documentation/130/cfx_ref.pdf Accessed Nov. 25, 2013.
25. Hunt, J.C.R.; Wray, A.; and Moin, P.: Eddies, Stream, and Convergence Zones in Turbulent Flows. Center for Turbulence Research Report CTR-S88, 1988.
26. Ziefle, J.; and Kleiser, L.: Numerical Investigation of a Film-Cooling Flow Structure: Effect of Crossflow Turbulence. *J. Turbomach.*, vol. 135, no. 4, 2013, pp. 041001—041001-12.
27. Johnson, P.L.; and Shyam, V.: Large Eddy Simulation of a Film Cooling Flow Injected From an Inclined Discrete Cylindrical Hole Into a Crossflow With Zero-Pressure Gradient Turbulent Boundary Layer. NASA/TM—2012-217695, 2012. <http://ntrs.nasa.gov>
28. Jarrin, N., et al.: A Synthetic-Eddy Method for Generating Inflow Conditions for LES. *Internat. J. Heat Fluid Flow*, vol. 27, 2006, pp. 585–593.